Low-Profile Two-Port MIMO Terminal Antenna for Low LTE Bands with Wideband Multimodal Excitation

Hanieh Aliakbari [1,1] and Buon Kiong Lau [2]

[1]Lund University
[2]Affiliation not available

November 8, 2023

Abstract

Multiple-input multiple-output (MIMO) is a key

enabler for high data rates in mobile communications. However, it is challenging to design MIMO terminal antennas for LTE bands below 1 GHz, due to the conventional chassis offering only one resonant characteristic mode (CM). Recently, it was shown that minor structural changes can yield up to two additional resonant modes for designing two-port MIMO antennas. Nonetheless, the resulting bandwidth for the second port is relatively small. To simultaneously meet bandwidth and other practical requirements (including low profile and no off-ground clearance), a step-by-step approach for structural changes and feed design is applied in this work to exemplify the use of physical insights from CM analysis to achieve a competitive wideband two-port solution. The main novelty is that an entirely new mode is identified and appropriately tuned by structural modification for creating an additional resonance below 1 GHz. Moreover, two simple probe-feed ports are designed to jointly excite different subsets of four modes over frequency. In addition, far-field pattern orthogonality is guaranteed by the different phase shifts of the characteristic electric fields at the port locations. Furthermore, bulkier self-resonant antenna elements are avoided. To show design flexibility, a three-port version is also demonstrated.

Low-Profile Two-Port MIMO Terminal Antenna for Low LTE Bands with Wideband Multimodal Excitation

Hanieh Aliakbari, *Graduate Student Member, IEEE*, and Buon Kiong Lau, *Senior Member, IEEE*

***Abstract*—Multiple-input multiple-output (MIMO) is a key enabler for high data rates in mobile communications. However, it is challenging to design MIMO terminal antennas for LTE bands below 1 GHz, due to the conventional chassis offering only one resonant characteristic mode (CM). Recently, it was shown that minor structural changes can yield up to two additional resonant modes for designing two-port MIMO antennas. Nonetheless, the resulting bandwidth for the second port is relatively small. To simultaneously meet bandwidth and other practical requirements (including low profile and no off-ground clearance), a step-by-step approach for structural changes and feed design is applied in this work to exemplify the use of physical insights from CM analysis to achieve a competitive wideband two-port solution. The main novelty is that an entirely new mode is identified and appropriately tuned by structural modification for creating an additional resonance below 1 GHz. Moreover, two simple probe-feed ports are designed to jointly excite different subsets of four modes over frequency. In addition, far-field pattern orthogonality is guaranteed by the different phase shifts of the characteristic electric fields at the port locations. Furthermore, bulkier self-resonant antenna elements are avoided. To show design flexibility, a three-port version is also demonstrated.**

***Index Terms*—MIMO systems, terminal antennas, wideband antennas, complex correlation coefficient, characteristic modes.**

I. Introduction

MULTIPLE-input multiple-output (MIMO) technology enables data rate to scale linearly with the number of antennas for a fixed transmit power and bandwidth [1]. It is in widespread use in Long Term Evolution (LTE), IEEE 802.11ac and other wireless communication systems [1].

A. MIMO Terminal Antenna Design Challenges

Implementing more than one antenna port per band for MIMO operation is challenging in user terminals, especially in frequency bands below 1 GHz, due to their compact form factor [2]. The small electrical size of the terminal chassis offers limited degrees of freedom (in terms of the number of resonant modes) to fulfill strict requirements of orthogonal MIMO antenna and wideband design. Moreover, the current trend points to lesser space for antennas in smartphones, e.g., decreasing thickness and ground clearance. On the other hand, these lower bands are critical for reliable coverage, due to lower propagation losses and larger signal penetration.

In recent years, many MIMO terminal antennas have been proposed, e.g., [3]-[23]. For the designs above 1 GHz [3]-[9], low coupling and correlation can be more easily achieved across the antenna ports via space, angle or polarization diversities, due to the electrically larger chassis facilitating more resonant orthogonal radiation modes, i.e., characteristic modes (CMs) [9]. In fact, high-end smartphones are equipped with four-port MIMO antennas for higher LTE bands.

On the other hand, below 1 GHz, the largest dimension of the terminal chassis is typically less than half-wavelength ($\lambda_0/2$). This results in the chassis having only one resonant mode [10], [11] (often called fundamental chassis mode), which has a large bandwidth. Hence, early designs of two-port MIMO antennas often lead to either a narrowband solution for the second port, by avoiding the use of the wideband single resonant mode [10]-[12], or solutions that mainly excite the single-mode using both ports, which cause high coupling and correlation [17]-[20], [24]. The latter approach may require additional isolation improvement techniques to meet system specific isolation requirements [24]. In addition, the profile (thickness) of modern terminals is typically less than 10 mm, which is electrically very small for frequencies below 1 GHz. This requirement often necessitates larger off-ground clearance (typically ~15mm) as a tradeoff for acceptable bandwidth and MIMO performance. Because of the above fundamental challenges, MIMO terminal antennas for low LTE bands are so far confined to only two-port designs [10]-[23].

B. Asymmetric Bandwidth Two-Port Designs Below 1 GHz

CM analysis (CMA) has been used in [10]-[16] to reduce the correlation of the two ports in the low band. This is motivated by the far-field orthogonality of CMs, which offers an effective framework to design orthogonal MIMO antennas. In [10], it is shown a slot-monopole and a planar inverted-F antenna (PIFA) give the measured isolation and envelope correlation coefficient (ECC) of 13 dB and 0.04, if the slot monopole placed at a short end is used to excite the fundamental chassis mode, whereas the PIFA is located at the chassis center to avoid exciting the chassis mode. However, without using the chassis for radiation, the 6 dB bandwidth of the PIFA is as small as 1%, which is

Manuscript received June 12, 2020. This work was supported by Vetenskapsrådet under Grants No. 2010-00468 and No. 2018-04717.

The authors are with the Department of Electrical and Information Technology, Lund University, 221 00 Lund, Sweden (e-mails: hanieh.aliakbari_abar@eit.lth.se; buon_kiong.lau@eit.lth.se).

Color versions of one or more of the figures in this paper are available online at http://ieeexplore.ieee.org.

impractical. A magnetic antenna at either short end of the chassis can be used to replace the PIFA [11]. But again, since the magnetic antenna's location is chosen to avoid exciting the chassis, the high isolation of over 20 dB and low ECC of below 0.01 are obtained at the expense of small bandwidth (i.e., 2%).

To increase the bandwidth of the second port while retaining high isolation, two more modes were made resonant in the low band by chassis modification [13]. However, since only one of the two modes was utilized by the second port, the resulting bandwidth is still small (9%) and the profile is still large (8mm). In [14], both of the additional modes were tuned and excited for the second port, slightly increasing the bandwidth to 11%, but the profile is unchanged. Generally in [13]-[16], using different modes for each port in resulted in lower bandwidth for one of the ports. Whereas asymmetrical bandwidths may be suitable for early LTE releases (e.g., Rel. 8 only requires MIMO for the downlink), symmetrical bandwidths are utilized in later releases, e.g., Rel. 10 (LTE-Advanced), to improve the uplink.

C. Symmetric Bandwidth Two-Port Designs Below 1 GHz

In the meantime, several two-port designs that offer wide symmetric bandwidth and moderate to low correlation below 1 GHz were proposed [18], [21]-[23] (see Table I). These designs do not make use of CMA. However, each port in [18] is claimed to be exciting a combined current mode. Defined by means of observing the chassis' current distributions, the two combined modes are formed from the monopole antennas' self-resonant mode and the chassis' dipole mode. Even though the ECC is as high as 0.5 and the total efficiency relatively low (>46%) at the low LTE bands, this work shows that two different modes can be excited jointly at each port for MIMO operation, which also conveniently result in symmetric bandwidths.

TABLE I
RECENT AND PROPOSED TWO-PORT DESIGNS WITH SYMMETRIC BANDWIDTH.

Ref.	Antenna type	Chassis size (mm^2)	Profile/ height (mm)	Port spacing (λ_0)	BW (%)	Max $\|S_{21}\|$ (dB)/Max correlation	Ground clearance (mm)	Min η_t (%)
[18]	Dual-monopole	120 × 60	7	0.20	25	-6.5 / 0.5	12	46
[21]	2 IFAs at shorter sides	150 × 78	7	0.50	30	NA/0.1	16	45
[22]	Coupled-line+branches	153 × 77	7.5	0.52	30	-10/0.35	10	47
[23]	2 IFAs at longer sides	148 × 68	5	0.23	13*	-10 / 0.5	2	50
This work	**2 probe feeds**	**130 × 60**	**4**	**0.2**	**25**	**-13/0.15**	**None**	**67**
This work (v.2)	**2 probe feeds**	**150 × 78**	**4**	**0.26**	**30**	**-14.2 /0.08**	**None**	**72**

NB: NA (not available), η_t (measured total efficiency), BW (bandwidth).
* ON state BW (Fig. 7(a) in [23]). 30% bandwidth with ON/OFF switching.

In fact, the same principle has been demonstrated earlier using CMA at a higher frequency (2.3 GHz) [8], where two modes are simultaneously excited by two MIMO antenna ports. It is shown using modal weighting coefficients that pattern orthogonality between the ports is achieved by means of phase difference in the excitation of one of the two ports. These pioneering designs [8], [18] focus on the analysis of the antenna operation after the feeding ports are chosen, rather than directly applying this principle to design the feeds. Nevertheless, they provide the insight that it is not necessary to excite different CMs in different ports as in [13], [14]. Moreover, self-resonant antenna structures (e.g., PIFA, monopole and slot antennas), bulkier than non-resonant coupling elements, are typically used for excitation by at least one of the two ports [10]-[15], [18], [19], [21]-[23]. Hence, efforts were made to avoid using self-resonant structures in MIMO antennas [9], [26].

D. New Low-Profile, Symmetric Wideband Two-Port Design

Considering the limitations of the state-of-the-art solutions, we show in this article that CMA provides the physical insights needed to systematically transform the two-port MIMO antenna in [13], [14] to simultaneously meet the requirements of low profile, wideband, low coupling and correlation, no ground clearance and adding a third port for LTE coverage under 1 GHz. Bulkier self-resonant structure is also avoided.

Specifically, based on the addition of shorted strips (T-strips) along the longer sides of the flat chassis in [13], [14], the profile was reduced by folding the strips. The folding slightly increased the resonant frequency and decreased the modal bandwidth of the strip-induced mode. In addition, the center position of the shorting pin along each strip was adjusted to decrease the resonant frequencies and increase the bandwidth potential. Then, a slot was added to each of the two longer sides of the chassis, just below the strips, to utilize an additional mode to enhance bandwidth at the higher frequency edge. Utilizing mainly those three resonant modes over the desired frequency range, two probe feeds were designed to replace the shorting pins to capacitively couple power into these modes to achieve wideband behavior for both ports and low ECC over the operating band. The feed design ensures that the condition for orthogonality is retained over the entire band of interest. In particular, the chosen feed location excites one mode with the same phase but the other mode in an out-of-phase fashion. This feeding approach is simple and it does not require a complex feeding network or power divider as utilized in [25] for modal excitation.

To our knowledge, the proposed antenna is the first low profile (4 mm), on-ground (i.e., no ground clearance) design that concurrently provides low correlation (ECC<0.15) and wide bandwidth of 0.75-0.96 GHz (25%) over the low LTE band (see "This work" in Table I). Moreover, the two ports are spaced by only $0.2\lambda_0$ and no switch or decoupling structure is needed. It is also noted that a typical mid-size chassis, smaller than those of [21]-[23], is used for our reference design. A larger chassis tends to improve bandwidth potential at the lower frequency edge, thus enabling a larger bandwidth, as confirmed by the simulated results of applying the proposed design steps on the larger chassis size of [21] (see "This work (v.2)" in Table I). To highlight another advantage of the design, which does not occupy either the top or bottom part of the chassis normally reserved for conventional self-resonant antennas, a third port is added to the top end to create a low-band three-port MIMO antenna, for the first time. The third port consists of a frequency tunable narrow-band antenna [11], which has little effect on the

existing ports. Further, it is noted that an early version of our proposed design has only 11% simulated bandwidth (0.85-0.95 GHz) [27]. The relatively poor performance is due to the new resonant mode introduced by the slots in the chassis not being utilized by this early design to enhance bandwidth, which is rectified in this work by means by detailed step-by-step CMA.

II. MIMO Analysis using Characteristic Mode Theory

In this section, CMA is briefly revisited, in the context of MIMO antenna design. CMs are real current modes that can be computed numerically for conducting bodies of arbitrary shape, obtained by solving the weighted eigenvalue equation [28]

$$X\mathbf{J}_n = \lambda_n R\mathbf{J}_n, \tag{1}$$

where $\mathbf{J}_n$ is the nth characteristic current associated with the nth eigenvalue λ_n. R and X are the real and imaginary parts of the symmetric impedance operator Z. Specifically, the CM far-fields produced by $\mathbf{J}_n$ are orthogonal to each other [28]. Thus, for the electric farfield $\mathbf{E}_n$

$$\frac{1}{2Z_0}\left\langle \mathbf{E}_m, \mathbf{E}_n^* \right\rangle = \delta_{mn} = \begin{cases} 1, & m = n \\ 0, & m \neq n \end{cases}, \tag{2}$$

where δ_{mn} is the Kronecker delta and Z_0 is the wave impedance of free space and * denotes complex conjugate operation. Also, the symmetric product of the two vector functions in (2), for $\mathbf{A}$ and $\mathbf{B}$ on the surface at infinity S_∞ (i.e., far-field) is defined as

$$\left\langle \mathbf{A}, \mathbf{B} \right\rangle = \iint_{S_\infty} \mathbf{A} \cdot \mathbf{B}^* ds. \tag{3}$$

The orthogonality feature of CM far-fields is ideally suited for MIMO antenna design and analysis. This is because MIMO systems (e.g., LTE) are typically used in rich multipath environments, where the angular power spectrum of the outgoing or incoming signal is nearly uniform. In such a propagation environment, orthogonal patterns of MIMO antenna elements are sufficient to guarantee uncorrelated signals across the antenna ports [2]. Therefore, as long as each antenna port excites one or more than one unique modes, with no mode being excited by more than one port, all the resulting patterns will be pairwise uncorrelated, as illustrated by (2), and likewise the received signals at antenna ports will be pairwise uncorrelated.

However, selective excitation of resonant CMs is sufficient, but not necessary to guarantee orthogonal antenna ports, as explained in the following. Consider a P-port MIMO antenna (P = 2 in this work), $\mathbf{E}^p$ is denoted as the excited electric field (E-field), when the pth port is excited by an impressed E-field $\mathbf{E}_i^p$. Since CM far-fields form a set of orthogonal functions, they can be used to expand the excited field $\mathbf{E}^p$ [28]

$$\mathbf{E}^p = \sum_{n=1}^{\infty} \alpha_{n,p}\mathbf{E}_n \approx \sum_{n=1}^{N} \alpha_{n,p}\mathbf{E}_n \tag{4}$$

where N is the number of dominating modes (with small absolute values of λ_n) and $\alpha_{n,p} = \left\langle \mathbf{J}_n, \mathbf{E}_i^p \right\rangle / (1 + j\lambda_n)$ denotes the modal weighting coefficient of the nth CM for the pth port.

To evaluate the magnitude and phase of the contribution of the nth CM to the far-field radiation pattern of the pth port, the complex correlation coefficient (CCC) between $\mathbf{E}^p$ and $\mathbf{E}_n$ is given by [29]

$$\rho_{n,p} = \alpha_{n,p} / \sqrt{P_{rad}}, \tag{5}$$

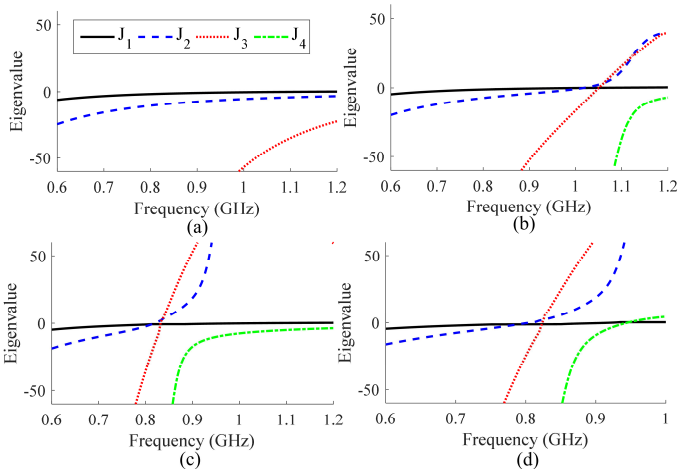

Fig. 1. Eigenvalues of four CMs of interest for the: (a) chassis, (b) chassis with folded strips and center shorting pins, (c) chassis with folded strip and offset shorting pins on the same side, (d) slotted chassis with folded strip and offset shorting pins in same side. Only modes relevant to the design are shown.

where P_{rad} is the constant total radiated power at each port, and the power budget implies that

$$\sum_{n=1}^{N} \left|\rho_{n,p}\right|^2 \approx 1. \tag{6}$$

Using (4), if P = 2 and N = 2, the E-fields for the ports are

$$\begin{aligned} \mathbf{E}^1 &= \alpha_{1,1}\mathbf{E}_1 + \alpha_{2,1}\mathbf{E}_2 \\ \mathbf{E}^2 &= \alpha_{1,2}\mathbf{E}_1 + \alpha_{2,2}\mathbf{E}_2 \end{aligned}, \tag{7}$$

The CCC of the far-field patterns for ports becomes

$$\begin{aligned} \rho_{\mathbf{E}^1,\mathbf{E}^2} &= \frac{\left\langle \mathbf{E}^1, \mathbf{E}^2 \right\rangle}{\sqrt{\left\langle \mathbf{E}^1, \mathbf{E}^1 \right\rangle \left\langle \mathbf{E}^2, \mathbf{E}^2 \right\rangle}} = \frac{\alpha_{1,1}\alpha_{1,2}^* + \alpha_{2,1}\alpha_{2,2}^*}{\sqrt{\left|\alpha_{1,1}\right|^2 + \left|\alpha_{2,1}\right|^2}\sqrt{\left|\alpha_{1,2}\right|^2 + \left|\alpha_{2,2}\right|^2}} \\ &= \rho_{1,1}\rho_{1,2}^* + \rho_{2,1}\rho_{2,2}^*. \end{aligned} \tag{8}$$

Therefore, in the equivalent context of modal currents, the individual terms $\alpha_{1,1}\alpha_{1,2}^*$ and $\alpha_{2,1}\alpha_{2,2}^*$ do not need to be zero for the sum to be zero, i.e., the general case when ports 1 and 2 do not excite different modes. For example, if ports 1 and 2 excite modes 1 and 2 by the same magnitude ($\left|\alpha_{1,1}\right| = \left|\alpha_{2,1}\right| = \left|\alpha_{1,2}\right| = \left|\alpha_{2,2}\right|$), but in a co-phase manner at port 1 ($\angle\alpha_{1,1} = \angle\alpha_{1,2}$) and 180° out-of-phase at port 2 ($\angle\alpha_{2,1} = \angle\alpha_{2,2} + \pi$), then $\rho_{\mathbf{E}^1,\mathbf{E}^2} = 0$ despite nonzero individual terms.

Another important point in CMA is that the tracking of eigenvalues obtained from (1) over a wide frequency band is very challenging, especially when new modes are introduced by chassis modification [13]-[15], [26]. The orthogonality of far-field patterns in (2) at a given frequency is also a suitable property to be used for modal tracking [30]. The eigenvalues of four CMs of interest in this work (see Fig. 1) were classified by the far-field tracking method of [30], which correlates the far-field patterns of each individual mode over frequency. The method was also applied for MIMO antenna design [14]. In contrast, in the preliminary study [27], a current-based tracking method [26] was used, and it failed to identify and track one of the modes, resulting in the missing mode ($\mathbf{J}_4$) not being used to enhance bandwidth.

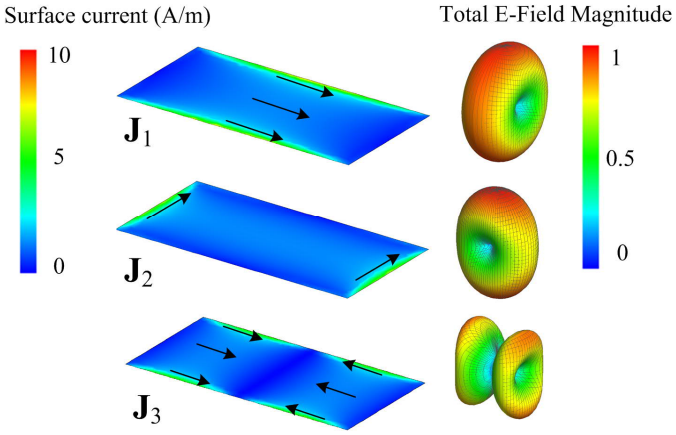

Fig. 2. Eigencurrent distribution and normalized pattern of CMs in the chassis with resonant frequencies of: 1.08 GHz ($\mathbf{J}_1$), 2.85 GHz ($\mathbf{J}_2$), 2.5 GHz ($\mathbf{J}_3$).

III. CM Modification and Excitation

In Fig. 1, the evolutions of the CMs of interest with minor chassis modifications for the entire design procedure are summarized in eigenvalue plots. The size of the terminal chassis was chosen to be 130 mm × 60 mm, intended for a typical mid-size smartphone. It is noted that the overall *outer* dimensions of a smartphone are bigger than those of its chassis. As the first design step, the characteristic eigenvalues for the 130 mm × 60 mm perfect electric conductor (PEC) chassis were computed and shown in Fig. 1(a). As can be seen, the chassis supports only one resonant mode ($\mathbf{J}_1$) close to 1 GHz. Two non-resonant modes of interest to this study ($\mathbf{J}_2$ and $\mathbf{J}_3$) are also shown in Fig. 1(a). In Fig. 2, the currents and the corresponding electric far-field patterns of $\mathbf{J}_1$ to $\mathbf{J}_3$ are shown as a reference. It can be seen that mode 1 ($\mathbf{J}_1$) is the fundamental dipole mode, with a current flowing along the length of the chassis. Mode 2 ($\mathbf{J}_2$) supports a current distribution like a dipole oriented along the chassis width. Mode 3 ($\mathbf{J}_3$) is a longitudinal full-wave dipole mode. The plain chassis is then modified in stages to obtain the desired characteristic properties, as will be described in this section. Figures 3(a)-3(c) illustrate the currents and electric far-field patterns of the CMs associated with the eigenvalues in Fig. 1(b)-(d), respectively, for different design stages.

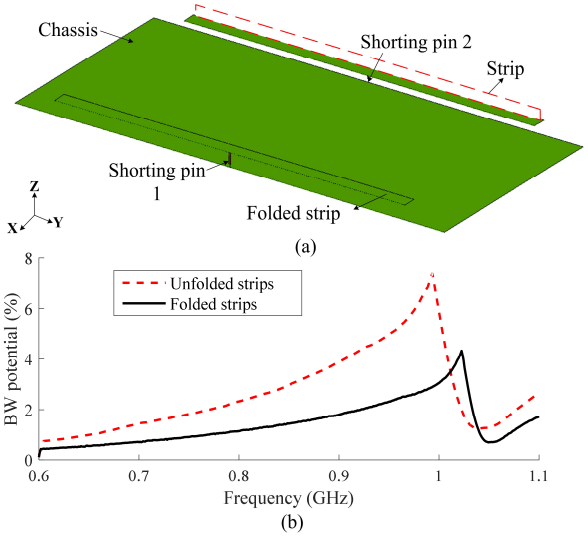

Fig. 4. (a) Chassis layout with unfolded (dashed outline)/folded (solid outline) strips at the two longer sides and with center shorting pins, (b) bandwidth potential of center excited probe feed with unfolded/folded strips.

A. Folding of T-Strips and Center Feed Positions

It is known that capacitive loading along the longer sides of the flat chassis using shorted metal strips (T-strips) enables two additional modes to be resonant below 1 GHz [13], [14], apart from the fundamental dipole mode. Specifically, these are the dipole mode along the width of the chassis as well as a mode resulting from the slots formed between the chassis and the shorted metal strips. However, as described earlier, the proposed antennas in [13] and [14] offer only a modest bandwidth (of up to 11%), with asymmetric bandwidths obtained across the two ports. Moreover, they require a profile of 8 mm and the addition of capacitive coupling elements

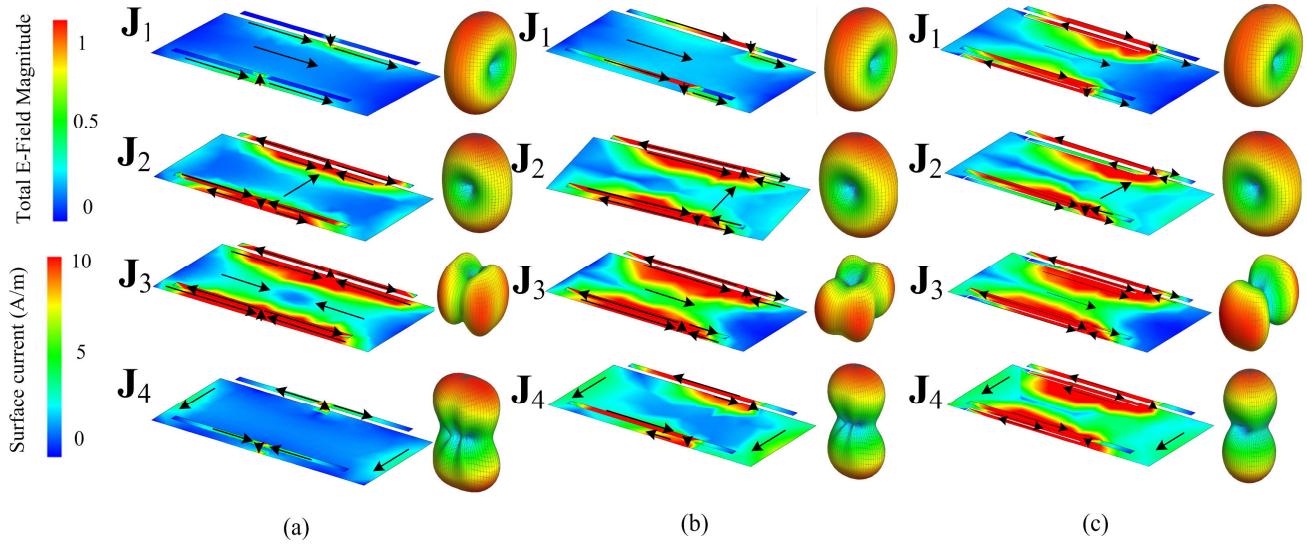

Fig. 3. Eigencurrent distribution and normalized pattern of CMs of chassis with folded strips and (a) center shorting pins with resonant frequencies of: 1.08 GHz ($\mathbf{J}_1$), 1.01 GHz ($\mathbf{J}_2$), 1.05 GHz ($\mathbf{J}_3$), 2.8 GHz ($\mathbf{J}_4$), (b) offset shorting pins in the same side with resonant frequencies of 1.08 GHz ($\mathbf{J}_1$), 0.8 GHz ($\mathbf{J}_2$), 0.83 GHz ($\mathbf{J}_3$), 1.84 GHz ($\mathbf{J}_4$), and (c) offset shorting pins in the same side with extra slot on the chassis with resonant frequencies of 1.02 GHz ($\mathbf{J}_1$), 0.78 GHz ($\mathbf{J}_2$), 0.83 GHz ($\mathbf{J}_3$), 0.94 GHz ($\mathbf{J}_4$).

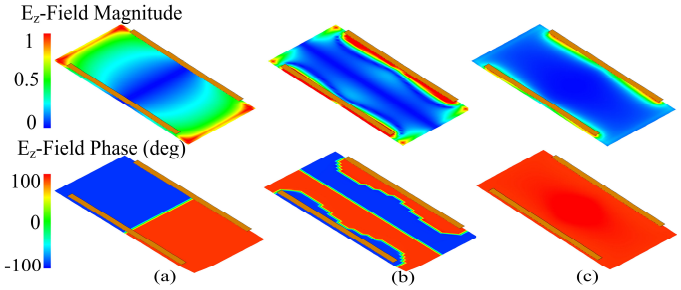

Fig. 5. Magnitude and phase of *z*-directed modal E-field distribution of (a) $\mathbf{J}_1$, (b) $\mathbf{J}_2$, and (c) $\mathbf{J}_3$, 2 mm above the chassis at resonant frequencies.

(CCEs) and/or off-ground self-resonant antenna elements. In this work, the chassis structure with T-strips (shorted in the center) in [13] was adopted as the initial design, based on which all of its limitations were addressed in the following step-by-step design procedure.

The first step was to lower the profile of the chassis structure by folding the T-strips into horizontal orientations, as shown in Fig. 4(a). This lowered the overall profile to 4 mm. The resulting eigenvalues, depicted in Fig. 1(b), reveal that the three resonant modes under 1 GHz (see Fig. 2(b) in [13]) are still available, despite the folding. However, by folding the strips, the resonant frequency of $\mathbf{J}_2$ approaches that of $\mathbf{J}_3$, and the maximum bandwidth potential [31] of the folded structure (with a shorting pin replaced by a probe feed) reduces from 7% to 4.3% (see Fig. 4(b), calculated using BetaMatch) and the frequency of maximum bandwidth potential increases from 0.99 to 1.02 GHz. In addition, as seen in Fig. 1(b), the slopes of $\mathbf{J}_2$ and $\mathbf{J}_3$ are steep (steeper than those of the unfolded case shown in Fig. 2(b) of [13]), whereas that of $\mathbf{J}_1$ is unchanged with the folding. Moreover, $\mathbf{J}_4$ has large eigenvalues below 1 GHz.

Figure 3(a) shows the corresponding eigencurrents and far-field patterns for the chassis with folded strips and centered shorting pins. $\mathbf{J}_1$ has strong currents along the two longer sides of the chassis, giving the classic half-wave dipole pattern along the chassis length. This verifies that the $\mathbf{J}_1$ is the fundamental dipole mode of the chassis. $\mathbf{J}_2$ has strong currents flowing along the strips and the chassis underneath them, due to the capacitive loading of the strips. However, these currents flow in opposite directions, hence it is the currents along the chassis width that contributes to the dipole pattern. In comparison to $\mathbf{J}_1$ and $\mathbf{J}_4$, the currents in the $\mathbf{J}_2$ and $\mathbf{J}_3$ are stronger around the metal strips and shorting pins. Nonetheless, the far-field patterns of $\mathbf{J}_2$ and $\mathbf{J}_3$ are different, since the currents' directions at two shorting pins are opposite in $\mathbf{J}_2$, but the same in $\mathbf{J}_3$. In contrast to $\mathbf{J}_1$, the far-field patterns of $\mathbf{J}_2$ and $\mathbf{J}_4$ are both along the chassis width; however, it is more directional for $\mathbf{J}_4$, since the currents on the strips also contribute to the pattern.

Figure 5 shows the magnitude and phase of the *z* component of the E-field 2 mm above the chassis for the first three modes (i.e., $\mathbf{J}_1$-$\mathbf{J}_3$). As shown in Fig. 5(b), it is expected that if the shorting pins in the center of the chassis are replaced by two (z-oriented) feeding ports (unmatched, unless otherwise stated), the electric near-field excitation of $\mathbf{J}_2$ by ports 1 and 2 will be 180° out-of-phase. In contrast, as shown in Fig. 5(c), $\mathbf{J}_3$ is excited by the two ports without any phase shift. Moreover, as the fundamental mode ($\mathbf{J}_1$) has a lower E-field magnitude at the

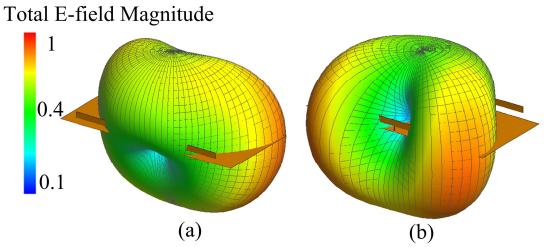

Fig. 6. 3D normalized radiation pattern by exciting individual ports at 1.04 GHz: (b) Port 1; (c) Port 2.

TABLE II
CCC BETWEEN EMBEDDED RADIATION PATTERNS AND CHARACTERISTIC FAR-FIELD PATTERNS IN FIG. 3(A).

	Mode 1	**Mode 2**	**Mode 3**
@1.02 GHz			
Port 1	0.05∠0°	0.97∠-16.4°	0.24∠-96°
Port 2	0.05∠180°	0.97∠163°	0.24∠-96°
@1.04 GHz			
Port 1	0.01∠-4.6°	0.72∠-55.3°	0.69∠73.8°
Port 2	0.01∠178°	0.72∠123.2°	0.69∠73.8°
@1.05 GHz			
Port 1	0.02∠-11°	0.3∠39°	0.95∠-65.8°
Port 2	0.02∠168°	0.3∠-148°	0.95∠-65°

ports, as compared with those of $\mathbf{J}_2$ and $\mathbf{J}_3$ (see Fig. 5(a)), the contribution of $\mathbf{J}_1$ to the overall radiation should be low. This can be confirmed by computing the magnitude and phase of the CCC using (5) for each port at three different frequencies around the resonances of $\mathbf{J}_2$ and $\mathbf{J}_3$ (see Table II). The percentage power in each mode for a given port is given by the magnitude square of the CCC. i.e., $|\rho_{p,n}|^2$. From Table II, it is computed that 99% of the total radiation power in each port is radiated by $\mathbf{J}_2$ and $\mathbf{J}_3$, with little contribution from $\mathbf{J}_1$. As expected from Fig. 5(b), it is confirmed in Table II that the excitation of $\mathbf{J}_2$ by ports 1 and 2 are 180° out-of-phase and $\mathbf{J}_3$ is excited in-phase.

Due to the lower eigenvalue of $\mathbf{J}_2$ at 1.02 GHz, it has more contribution to the far-field patterns than $\mathbf{J}_3$. Hence, the total patterns of both ports are similar to the pattern of $\mathbf{J}_2$, indicating high correlation. However, at 1.04 GHz, the far-field patterns are almost equally contributed by $\mathbf{J}_2$ and $\mathbf{J}_3$, with 180° phase difference in the excitation of $\mathbf{J}_2$ by the two ports. Thus, the CCC of the two ports is nearly zero at 1.04 GHz. The pattern orthogonality can be visualized by significant differences in the far-field patterns of the two unmatched ports (see Fig. 6). However, as the frequency increases further to 1.05 GHz, the patterns of two ports are dominated by $\mathbf{J}_3$, degrading the pattern orthogonality of the two ports. Therefore, it is concluded that pattern orthogonality is only achieved for a small bandwidth. Moreover, as mentioned, Fig. 4(a) shows that the maximum bandwidth that can be achieved for the folded strips' case with the center-feed ports is also small 4.3%. To match both ports at the frequency of maximum bandwidth potential (1.02 GHz, see Fig. 4(a)), a two Murata element matching network consisting of a parallel inductor (L = 2 nH) and a series capacitor (C = 12 pF) was used at each port.

Although the folding the strips has resulted in a smaller bandwidth (from 7% to 4.3%) and poor ECC performance, the

performance limitation is mostly due to the two center-feed ports not exciting the wideband $\mathbf{J}_1$ mode. Therefore, to enlarge the bandwidth, $\mathbf{J}_1$ should also be excited by two ports.

B. *Offset Feed Positions*

To utilize $\mathbf{J}_1$, it is necessary to offset the two feeding ports (probe feeds) from the center of the strips, so to excite its electric near-field (see magnitude distribution of Fig. 5(a)). Based on this consideration, there are two options, i.e., offsetting the two ports from the center position in the same or the opposite directions along the longer sides. However, from the phase response of Fig. 5(a), it can be seen that these two cases differ in that the same-direction offset results in in-phase excitation of $\mathbf{J}_1$, whereas the opposite-direction offset result in 180° out-of-phase excitation. On the other hand, both offset cases result in equal magnitude but 180° out-of-phase excitation of $\mathbf{J}_2$ (see Fig. 5(b)). Therefore, according to (8) as well as the discussions in Section II, the same-direction offset should provide low correlation between the two ports, whereas the opposite-direction offset should result in high correlation. These predictions are verified in Fig. 7(b), where the ECC exceeds 0.4 for the opposite-direction case but lower than 0.1 for the same-direction offset, within their respective 6 dB impedance bandwidth. As before, both ports in the same-direction offset case were matched at the frequencies of maximum bandwidth (0.8 GHz) with two Murata element matching networks. The parallel inductor value and the series capacitor value were 3.4 nH and 11.4 pF, respectively. Relative to the center fed chassis, the maximum bandwidth potential with the same-direction offset feed increases from 4.3% to 7%, due to the excitation of $\mathbf{J}_1$. Also, as shown in Fig. 7(b), the isolation is larger than 9 dB in the bandwidth (0.77-0.83 GHz).

For further validation of the same-direction offset case, the CCC between each mode and each port was calculated using (5) and summarized in Table III at three frequencies within the 6 dB impedance bandwidth. Similar to the previous case in Table II, it can be observed that $\mathbf{J}_2$ is excited with 180° phase shift and $\mathbf{J}_3$ is excited in phase between the ports. However, contrary to the center-feed chassis, the contribution of $\mathbf{J}_1$ is higher, and it is excited in-phase by the two ports (as expected from Fig. 5(a)). Moreover, the excitation of $\mathbf{J}_3$ is less than that of $\mathbf{J}_1$ and $\mathbf{J}_2$ in the band because of $\mathbf{J}_3$'s narrower bandwidth (compare Figs. 1(b) and 1(c)). Therefore, the total patterns (see Fig. 8) is a combination of the far-field dipole patterns of $\mathbf{J}_1$ and $\mathbf{J}_2$, with a rotation of $\phi \approx 45°$ relative to either modal pattern.

Furthermore, it is shown in Fig. 3(b) that by moving the shorting pins from the center, $\mathbf{J}_1$ has more surface currents around the metal strips and shorting pins (than that in Fig. 3(a)). Compared to the center shorting pins, due to the longer slots formed between the metal strips and the chassis, the resonance frequency of the $\mathbf{J}_2$ and $\mathbf{J}_3$ will shift to lower frequencies and resonance of the $\mathbf{J}_1$ remains almost unchanged (see Fig. 1(c)). The resonant frequency of $\mathbf{J}_4$ is also reduced but it is still far those of the other three modes (i.e., $\mathbf{J}_1$, $\mathbf{J}_2$ and $\mathbf{J}_3$ resonate under 1 GHz). However, in comparison to Fig. 1(b), the slope of $\mathbf{J}_3$ is larger in Fig. 1(c), thus its modal bandwidth is smaller. The resonant frequency of $\mathbf{J}_2$ and $\mathbf{J}_3$ can be tuned with the longer slots (i.e., L_2 in Fig. 10) on both sides.

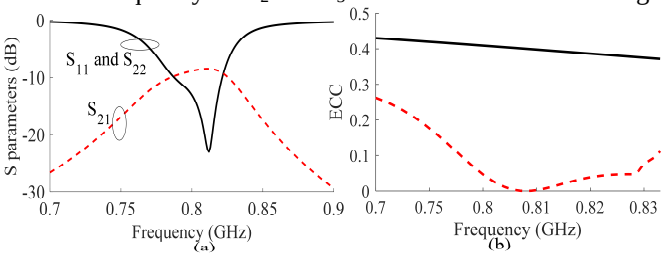

Fig. 7. (a) S parameters of the two matched ports for the offset feed in the same direction and (b) ECC of two matched ports in the operating bandwidth for offset feed in opposite direction (solid) and same direction (dashed).

TABLE III
CCC BETWEEN EMBEDDED RADIATION PATTERNS AND CHARACTERISTIC FAR-FIELD PATTERNS OF FIG. 3(B).

	Mode 1	**Mode 2**	**Mode 3**
@0.79 GHz			
Port 1	0.68∠43.6°	0.72∠36°	0.16∠-92°
Port 2	0.68∠43°	0.72∠-137°	0.16∠-92°
@0.82 GHz			
Port 1	0.70∠25.9°	0.68∠-31.6°	0.2∠51.4°
Port 2	0.70∠24°	0.68∠140°	0.2∠51.4°
@0.83 GHz			
Port 1	0.61∠26.1°	0.66∠118°	0.43∠79.3°
Port 2	0.61∠25°	0.66∠-75°	0.43∠79.3°

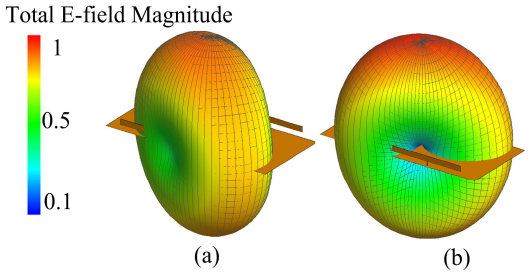

Fig. 8. 3D normalized radiation pattern by exciting individual ports at 0.83 GHz: (a) port 1; (b) port 2.

Despite the good ECC performance of the same-direction offset feed structure shown in Fig. 7(b), the bandwidth of 7% (see Fig. 7(a)) is still small and cannot cover the low LTE bands. The isolation performance is likewise only moderate (above 9 dB). Furthermore, even though the impedance bandwidth can be increased using more complex matching networks in BetaMatch (10% bandwidth was achieved with four matching elements), the ECC will increase towards the lower frequencies (e.g., 0.75 GHz) and higher frequencies (e.g., 0.96 GHz). This is because the excitation of $\mathbf{J}_2$ will decrease in those frequencies and $\mathbf{J}_1$ is the only mode which will be excited by the two ports.

C. *Slotted Chassis*

To increase the bandwidth of both ports at the higher frequency edge, while retaining low ECC, another mode needs to be jointly excited alongside with $\mathbf{J}_1$, to replace the role of $\mathbf{J}_2$ at lower frequencies. Since the E-fields of $\mathbf{J}_1$ excited by the two offset feeds are of equal magnitude and phase (with the feed positions chosen for proper lower frequency excitation of $\mathbf{J}_1$ and $\mathbf{J}_2$), the two feeds should excite the E-fields of the new mode with equal magnitude and 180° out-of-phase at the two feeds

(as was the case for $\mathbf{J}_2$) to ensure that ECC is low, as predicted

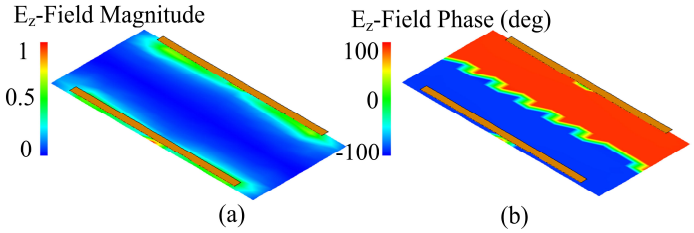

Fig. 9. (a) Magnitude, and (b) phase of z-directed modal E-field of $\mathbf{J}_4$, 2 mm above the chassis at resonant frequencies.

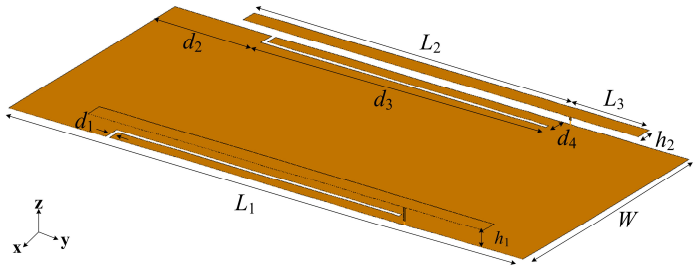

Fig. 10. Final simulated prototype with the total dimensions of 130 × 60 × 4 mm^3. The design parameters are: L_1 = 130 mm, L_2 = 81 mm, L_3 = 20 mm, h_1 = 4 mm, h_2 = 4 mm, d_1 = 1 mm, d_2 = 27 mm, d_3 = 74 mm, d_4 = 3 mm, W = 60 mm.

TABLE IV
CCC BETWEEN EMBEDDED RADIATION PATTERNS AND CHARACTERISTIC FAR-FIELD PATTERNS OF FIG. 3(C).

@0.82 GHz	**Mode 1**	**Mode 2**	**Mode 3**	**Mode 4**
Port 1	0.68<5.6°	0.72<-29.4°	0.13<-93.9°	0.1<-90.5°
Port 2	0.69<5.7°	0.69<151°	0.13<-93.9°	0.12<89.5°
@0.75 GHz				
Port 1	0.65 <-79.9°	0.71<-160°	0.2<-42.5°	~0
Port 2	0.65<-79.9°	0.71<16.7°	0.2<-42.5°	~0
@0.94 GHz				
Port 1	0.69<-12.7°	~0	0.28<-89°	0.69<62.8°
Port 2	0.67<-15.6°	~0	0.22<-89°	0.70<-120°

by (8). As shown in Fig. 1(c), $\mathbf{J}_4$'s resonance is above 1 GHz, so by nature it cannot be used to extend the bandwidth and $\mathbf{J}_2$ has lower modal significance in higher frequencies. However, the E-field distribution of $\mathbf{J}_4$ has the desired property of being equal in magnitude but 180° out-of-phase at the feed locations, (see Fig. 9). This makes $\mathbf{J}_4$ a good candidate for the new mode.

Therefore, the structure should be modified to allow $\mathbf{J}_4$ to contribute to the radiation in the higher frequencies, alongside with $\mathbf{J}_1$. To this end, by inspecting the current distribution of $\mathbf{J}_4$ in Fig. 3(b), the resonant frequency of $\mathbf{J}_4$ can be decreased to below 1 GHz (i.e., 0.94 GHz) by inserting two slots along the longer sides of the chassis, as shown in Fig. 10. In this way, the current path along the chassis width is increased. Similarly, the resonant frequency of $\mathbf{J}_2$ is also decreased to 0.78 GHz, which can contribute to the radiation and improve the ECC at lower frequencies. By the length of this slot (i.e. d_3 in Fig. 10), the resonant frequency of $\mathbf{J}_4$ can be tuned. The computed CCC between each mode and each port is shown in Table IV for three frequencies. As can be seen, $\mathbf{J}_4$ offers almost equal contribution as $\mathbf{J}_1$ in magnitude, but nearly 180° out-of-phase excitation as compared to $\mathbf{J}_1$'s nearly co-phase excitation. Furthermore, by adding the slot, the frequency of maximum bandwidth potential increases to 0.9 GHz, and the bandwidth potential improves because of one more resonant mode: $\mathbf{J}_4$ adds some reactive

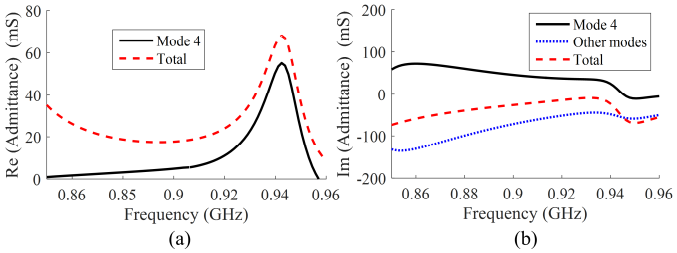

Fig. 11. (a) Real part and (b) Imaginary part of the modal and total admittance.

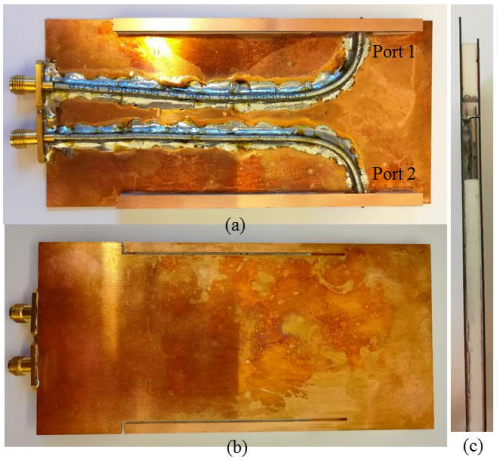

Fig. 12. Fabricated two-port prototype: (a) top, (b) back and (c) side views.

admittance (see Fig. 11(b)) to the other modes' reactive admittances and also increases the real part of input admittance at the higher frequencies (see Fig. 11(a)).

Finally, both ports were matched using the BetaMatch software. To match the ports, a three element ∏ matching network consisting of a 4.3 nH series Murata inductor together with 18 pF and 10 pF parallel Murata capacitors was used. One more matching element was used here than the previous cases (in Section III-A and Section III-B), as it was needed to improve the matching at the lower frequencies.

IV. PROTOTYPE VERIFICATION

The proposed antenna was fabricated, as shown in Fig. 12. A copper plate (thickness of 0.5 mm) was used as the chassis of the prototype and Rohacell foams were used to keep the feeding structures at the two longer sides more stable. The foams are electrically neutral (ε_r = 1), so it does not load the modes and change the simulated results. The feed cables were well soldered to the chassis to mitigate cable influence. The simulated and measured S parameters agree well (see 13(a)). The final design provides the 6 dB impedance bandwidths of 0.75-0.96 GHz (25%). The measured far-field patterns, shown in Fig. 14, illustrate that a high level of orthogonality is achieved between the two ports at three sample frequencies. The measured ECC is below 0.15 (see Fig. 13(b)) and the measured total efficiency is above 67% (average of 71%) over the impedance bandwidth.

V. FEASIBILITY OF THREE-PORT ANTENNA AT LOW FREQUENCY BAND

As mentioned earlier, one advantage of the proposed two-

port antenna is that it does not need to occupy the top or bottom

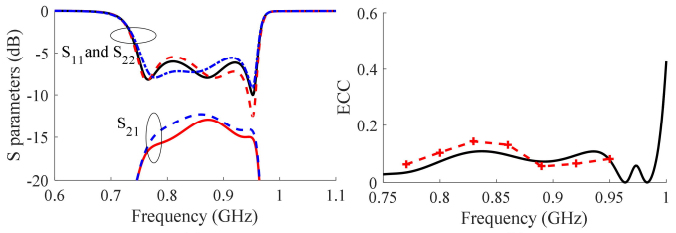

Fig. 13. (a) S parameters and (b) ECC of the simulated (solid lines) and measured (dashed lines) prototype of two-port antenna designed using CMA.

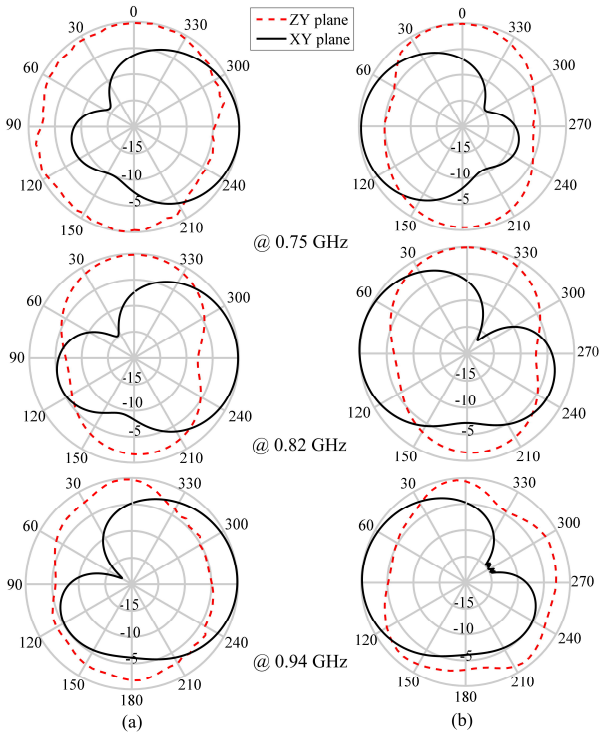

Fig. 14. Measured total radiation patterns of the two-port prototype at three frequencies: (a) port 1 excitation. (b) port 2 excitation.

end of the chassis, typically used for self-resonant antenna elements. Moreover, because of the chassis' electrically small dimensions, achieving more than two uncorrelated ports in the low frequency band is challenging. In [32], a four-port dual-band MIMO terminal antenna is formed using four non-resonant elements with 11 mm^2 of ground clearance. The bandwidth is 15% at the low band (824-960 MHz). Although all four ports mainly excite the fundamental mode of the large chassis (157 × 90 mm^2) at the lower band, the placement of the non-resonant elements at the four corners of the chassis helps to reduce the ECC. However, in part due to high coupling (up to -8 dB), the minimum port efficiency is only 24.9%.

In this section, extending the proposed two-port wideband design, the feasibility of a three-port structure for low band coverage is studied. In particular, the planar-coupled feed loop in [33] was employed to realize the self-resonant magnetic antenna as the third port. The loop antenna [33] was previously adopted in [11] to provide an uncorrelated but narrowband second port for a traditional chassis top/bottom antenna. The antenna occupies 15 mm × 60 mm at the top end of the two-

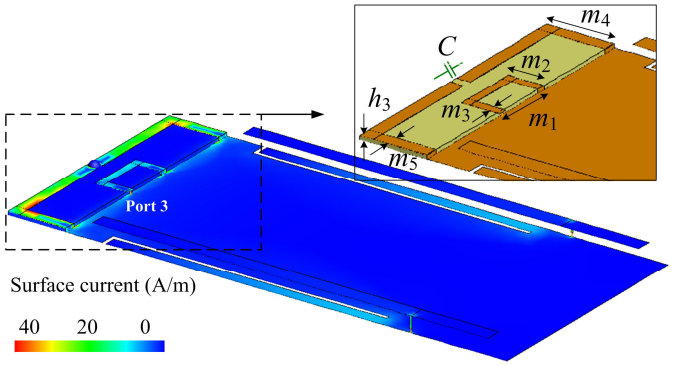

Fig. 15. Current distribution of the 3-port antenna at 0.95 GHz when the loop antenna is excited. The parameters of the loop antenna are: m_1 = 15 mm, m_2 = 10 mm, m_3 = 2 mm, m_4 = 15 mm, m_5 = 3 mm, h_3 = 0.8 mm, C = 0.17 pF. The substrate has a permittivity of 2.45, a loss tangent of 0.003 and a thickness h_3. All other dimensions are the same as those in Fig. 15.

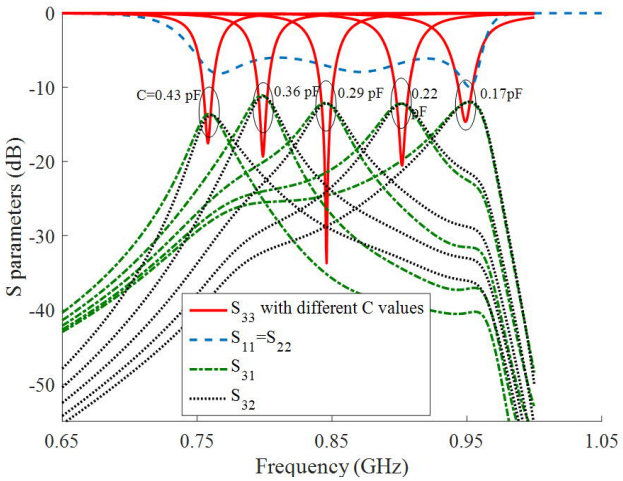

Fig. 16. Simulated S parameters of the coupled loop, with different values of C.

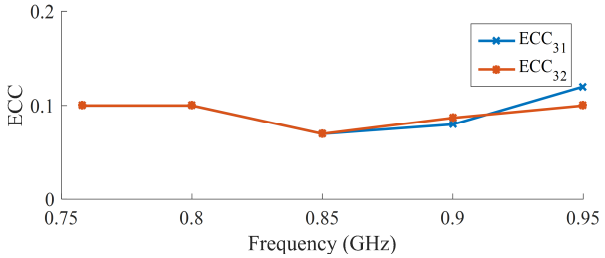

Fig. 17. Simulated ECC of the three port antenna based on far-field patterns.

port structure (see Fig. 15), with the total chassis length (130 mm) unchanged. As observed in Fig. 15, the coupled feed loop is implemented on a substrate and consists of two half-square rings, with the inner ring acting as the matching feed and the outer ring as the main radiator [33]. Although the coupled loop makes use of the shorter edge of the chassis, the resonant modes of the chassis is not excited over the existing two ports' 6 dB bandwidth (i.e., magnetic fields of $\mathbf{J}_1$-$\mathbf{J}_4$ are weak at this location). Therefore, only the loop is excited (as a self-resonant structure) and the current is mostly confined around the outer loop (see Fig. 15). Only small amounts of currents are coupled to the slots on the chassis. The parameters of the coupled loop antenna are shown in Fig. 16. It is noted that the operation of the ports 1 and 2 will not be affected by adding the third port so

the parameters of the chassis are the same as Fig. 10 and no re-optimization is needed.

A major drawback of the coupled loop antenna is the narrow bandwidth [11], [33]. However, it can still be used as a diversity antenna, where a relatively small instantaneous bandwidth is needed (e.g., up to 20 MHz for LTE). To provide coverage over the entire low band, the resonant frequency of the coupled loop antenna (or third port) can be tuned by replacing the fixed capacitor between the two-arm separations of the outer loop (i.e., *C* in Fig. 15) with a varactor. The S parameters with different capacitance values are shown in Fig. 16. The required tuning range of the varactor is between 0.17-0.43 pF to cover the bandwidth of the other two ports shown in Fig. 13(a). No matching network is needed. The achieved isolation is above 12 dB, which is enough for frequency bands below 1 GHz. More importantly, the ECC between the third port and any of the other ports is below 0.11 for all varactor states (see Fig. 17). The total simulated efficiency of port 3 is above 83% for all the different *C* values. Finally, it is noted that a fourth port can also be accommodated in the proposed design by adding another coupled loop antenna to the bottom end of the chassis in Fig. 15. This is possible due to the self-resonant coupled loop antenna not exciting the CMs utilized by the first two ports.

VI. Conclusion

This paper presents a concept design of MIMO terminal antennas that relies on the joint excitation of multiple chassis modes with proper phase shifts to drastically improve the impedance bandwidth in the low band while retaining low correlation. To this end, the characteristic currents as well as the amplitude and phase of the electric near-fields of the modes were used to guide the stepwise modifications of a previous strip-loaded chassis. The proposed low-profile two-port design, utilizing direct probe feeds at the loading strips and two added slots on the chassis, achieves the same bandwidth over both ports, covering 0.75-0.96 GHz (25% bandwidth). Moreover, utilizing a slightly larger chassis will allow the proposed design to cover the entire LTE low band 0.698-0.96 GHz (30%, see Table I). In addition, it is shown that a narrowband but tunable third antenna port can be added to the unused space typically occupied by traditional self-resonant antenna elements, to provide a three-port MIMO antenna. Possible future works include the enhancement of the bandwidth of the third port and the study of user effects on the proposed design using new CMA methods such as that proposed in [34].

Acknowledgment

The authors would like to thank Andreas Johansson at Lund University for his help in fabricating the antenna prototype.

References

[1] E. Dahlman, S. Parkvall, and J. Sköld, *4G LTE-Advanced Pro and The Road to 5G*, 3rd Ed., Academic Press, 2016.

[2] H. Li and B. K. Lau, "MIMO systems and antennas for terminals," in *Handbook of Antenna Technologies*, Z. N. Chen, Ed. Springer, 2015, pp. 1-35.

[3] M.-Y. Li et al., "Eight-port orthogonally dual-polarized antenna array for 5G smartphone applications," *IEEE Trans. Antennas Propag.*, vol. 64, no. 9, pp. 3820–3830, Sep. 2016.

[4] J. Guo, L. Cui, C. Li, and B. Sun, "Side-edge frame printed eight-port dual-band antenna array for 5G smartphone applications," *IEEE Trans. Antennas Propag.*, vol. 66, no. 12, pp. 7412–7417, Dec. 2018.

[5] Z. Qin, W. Geyi, M. Zhang, and J. Wang, "Printed eight-element MIMO system for compact and thin 5G mobile handset," *Electron. Lett.*, vol. 52, no. 6, pp. 416–418, Mar. 2016.

[6] G. Li et al., "Isolation-improved dual-band MIMO antenna array for LTE/WiMAX mobile terminals," *IEEE Antennas Wireless Propag. Lett.*, vol. 13, pp. 1128–1131, 2014.

[7] M. Ikram, R. Hussain, A. Ghalib, and M. S. Sharawi, "Compact 4-element MIMO antenna with isolation enhancement for 4G LTE terminals," in *Proc. IEEE Int. Symp. Antennas Propag. (APSURSI)*, Fajardo, Puerto Rico, Jun. 2016, pp. 535–536.

[8] K. K. Kishor and S. V. Hum, "A two-port chassis-mode MIMO antenna," *IEEE Antennas Wireless Propag. Lett.*, vol. 12, pp. 690–693, 2013.

[9] R. Martens and D. Manteuffel, "Systematic design method of a mobile multiple antenna system using the theory of characteristic modes," *IET Microw. Antennas Propag.*, vol. 8, no. 12, pp. 887 – 893, 2014.

[10] H. Li, et al., "Characteristic mode based tradeoff analysis of antenna-chassis interactions for multiple antenna terminals," *IEEE Trans. Antennas Propag.*, vol. 60, no. 2, pp.490–502, Feb. 2012.

[11] H. Li, B. K. Lau, Z. Ying, and S. He, "Decoupling of multiple antennas in terminals with chassis excitation using polarization diversity, angle diversity and current control," *IEEE Trans. Antennas Propag*., vol. 60, no. 12, pp. 5947-5957, Dec. 2012.

[12] I. Szini, A. Tatomirescu, and G. F. Pedersen, "On small terminal MIMO antennas, harmonizing characteristic modes with ground plane geometry," *IEEE Trans. Antennas Propag*., vol. 63, no. 4, pp. 1487–1497, Apr. 2015.

[13] H. Li, Z. Miers, and B. K. Lau, "Design of orthogonal MIMO handset antennas based on characteristic mode manipulation at frequency bands below 1 GHz," *IEEE Trans. Antennas Propag*., vol. 62, no. 5, pp. 2756-2766, May 2014.

[14] Z. Miers, H. Li, and B. K. Lau, "Design of bandwidth enhanced and multiband MIMO antennas using characteristic modes," *IEEE Antennas Wireless Propag. Lett*., vol. 12, pp. 1696–1699, 2013.

[15] C. Deng, Z. Feng, and S. V. Hum, "MIMO mobile handset antenna merging characteristic modes for increased bandwidth," *IEEE Trans. Antennas Propag.*, vol. 64, no. 7, pp. 2660–2667, Jul. 2016.

[16] K. K. Kishor, and S. V. Hum, "Multiport multiband chassis-mode antenna design using characteristic modes," *IEEE Antennas Wireless Propag. Lett.*, vol. 16, pp. 609-612, 2017.

[17] A. A. Al-Hadi and R. Tian, "Impact of multiantenna real estate on diversity and MIMO performance in mobile terminals," *IEEE Antennas Wireless Propag. Lett*., vol. 12, pp.1712-1715, 2013.

[18] S. Zhang, K. Zhao, Z. Ying, and S. He, "Investigation of diagonal antenna–chassis mode in mobile terminal LTE MIMO antennas for bandwidth enhancement," *IEEE Antennas Propag. Mag.*, vol. 57, no. 2, pp. 217–228, Aug. 2015.

[19] Y. L. Ban, Z. X. Chen, Z. Chen, K. Kang, and J. L. W. Li, "Decoupled closely spaced heptaband antenna array for WWAN/LTE smartphone applications," *IEEE Antennas Wireless Propag. Lett*., vol. 13, pp. 31-34, 2014.

[20] J. Holopainen, J. Ilvonen, R. Valkonen, A. A. H. Azremi, and P. Vainikainen, "Study on the minimum required size of the low-band cellular antenna in variable-sized mobile terminals," in *Proc. 6th Eur. Conf. Antennas Propag. (EuCAP), Prague, Czech Republic*, Mar. 26-30, 2012, pp. 2754–2758.

[21] I. Barani, and K. Wong, "Integrated inverted-F and open-slot antennas in the metal-framed smartphone for 2 x 2 LTE LB and 4 x4 LTE M/HB MIMO operations," *IEEE Trans. Antennas Propag.*, vol. 66, no. 10, pp. 5004–5012, Oct. 2018.

[22] D. Huang, Z. Du, and Y. Wang. "A quad-antenna system for 4G/5G/GPS metal frame mobile phones," *IEEE Antennas Wireless Propag. Lett.*, vol. 18, no. 8, pp. 1586-1590, Aug. 2019.

[23] J. Choi, W. Hwang, C. You, B. Jung, and W. Hong, "Four-element reconfigurable coupled loop MIMO antenna featuring LTE full-band operation for metallic-rimmed smartphone," *IEEE Trans. Antennas Propag.*, vol. 67, no. 1, pp. 99–107, Jan. 2019.

[24] J. Ilvonen, J. Holopainen, K. Rasilainen, A. Lehtovuori and V. Viikari, "Suitable multiantenna placement in mobile handsets based on

electromagnetic isolation," in *Proc. 10th Europ. Conf. Antennas Propag. (EuCAP)*, Davos, Switzerland, Apr. 10-15, 2016, pp. 1-4.

[25] N. Peitzmeier and D. Manteuffel, "Upper bounds and design guidelines for realizing uncorrelated ports on multimode antennas based on symmetry analysis of characteristic modes," *IEEE Trans. Antennas Propag.*, vol. 67, no. 6, pp. 3902-3914, Jun. 2019.

[26] C. Deng, Z. Xu, Aidi Ren, and S. V. Hum, "TCM-based bezel antenna design with small ground clearance for mobile terminals," *IEEE Trans. Antennas Propag.*, vol. 67, no. 2, pp. 745-754, Feb. 2019.

[27] H. Li, and B. K. Lau, "Design of low profile MIMO antennas for mobile handset using characteristic mode theory," in *Proc. IEEE 5th Asia-Pacific Conf. Antennas Propag.*, Kaohsiung, Taiwan, Jul. 26-29, 2016, pp. 63-64.

[28] R. Harrington and J. Mautz, "Theory of characteristic modes for conducting bodies," *IEEE Trans. Antennas Propag.*, vol. AP-19, no. 5, pp. 622–628, Sep. 1971.

[29] E. Safin and D. Manteuffel, "Reconstruction of the characteristic modes on an antenna based on the radiated far field," *IEEE Trans. Antennas Propag.*, vol. 61, no. 6, pp. 2964–2971, Jun., 2013.

[30] Z. Miers and B. K. Lau, "Wide band characteristic mode tracking utilizing far-field patterns," *IEEE Antennas Wireless Propag. Lett.*, vol. 14, pp. 1658–1661, 2015.

[31] J. Villanen, J. Ollikainen, O. Kivekäs, and P. Vainikainen, "Coupling element based mobile terminal antenna structures," *IEEE Trans. Antennas Propag.*, vol. 54, no. 7, pp. 2142-2153, Jul. 2006.

[32] J. Anguera, A. Andújar, R. M. Mateos and S. Kahng, "A 4 × 4 MIMO multiband antenna system with non-resonant elements for smartphone platforms," in *Proc. 11th Europ. Conf. Antennas Propag. (EUCAP)*, Paris, France, Mar. 19-24, 2017, pp. 2705-2708.

[33] A. Erentok and R. W. Ziolkowski, "Metamaterial-inspired efficient electrically small antennas," *IEEE Trans. Antennas Propag.*, vol. 56, no. 3, pp. 691–707, Mar. 2008.

[34] P. Ylä-Oijala, A. Lehtovuori, R. Luomaniemi and V. Viikari, "Characteristic mode analysis of user's effect on mobile handset antennas," in *Proc. 13th Europ. Conf. Antennas Propag. (EuCAP)*, Krakow, Poland, Mar. 31-Apr. 5, 2019, pp. 1-4.